Since January 2020 Elsevier has created a COVID-19 resource centre with free information in English and Mandarin on the novel coronavirus COVID-19. The COVID-19 resource centre is hosted on Elsevier Connect, the company's public news and information website.

Sensors & Actuators: B. Chemical 351 (2022) 130897

Contents lists available at ScienceDirect

Sensors and Actuators: B. Chemical

journal homepage: www.elsevier.com/locate/snb

Rapid field determination of SARS-CoV-2 by a colorimetric and fluorescent dual-functional lateral flow immunoassay biosensor

Han Han [a,b], Chongwen Wang [b,c,*], Xingsheng Yang [b], Shuai Zheng [b,c], Xiaodan Cheng [b,c], Zhenzhen Liu [b], Baohua Zhao [a,**], Rui Xiao [b,**]

[a] College of Life Science, Hebei Normal University, Shijiazhuang 050024, PR China
[b] Beijing Institute of Radiation Medicine, Beijing 100850, PR China
[c] College of Life Sciences, Anhui Agricultural University, Hefei 230036, PR China

ARTICLE INFO

Keywords:
SARS-CoV-2 S1 protein
SiO_2@Au/QD
Dual-functional LFIA biosensor
Rapid and sensitive detection

ABSTRACT

The rapid and accurate diagnosis of severe acute respiratory syndrome coronavirus 2 (SARS-CoV-2) at the early stage of virus infection can effectively prevent the spread of the virus and control the epidemic. Here, a colorimetric and fluorescent dual-functional lateral flow immunoassay (LFIA) biosensor was developed for the rapid and sensitive detection of spike 1 (S1) protein of SARS-CoV-2. A novel dual-functional immune label was fabricated by coating a single-layer shell formed by mixing 20 nm Au nanoparticles (Au NPs) and quantum dots (QDs) on SiO_2 core to produce strong colorimetric and fluorescence signals and ensure good monodispersity and high stability. The colorimetric signal was used for visual detection and rapid screening of suspected SARS-CoV-2 infection on sites. The fluorescence signal was utilized for sensitive and quantitative detection of virus infection at the early stage. The detection limits of detecting S1 protein via colorimetric and fluorescence functions of the biosensor were 1 and 0.033 ng/mL, respectively. Furthermore, we evaluated the performance of the biosensor for analyzing real samples. The novel biosensor developed herein had good repeatability, specificity and accuracy, which showed great potential as a tool for rapidly detecting SARS-CoV-2.

1. Introduction

The 2019 coronavirus disease (COVID-19) is highly infectious, highly pathogenic, and has a high mortality rate that has caused a serious health problem worldwide. In the early stages of infection, patients often exhibit functional symptoms similar to those of ordinary flu, such as fever and dry cough. As viral infection progresses to the lower trachea and even to the lungs, the disease rapidly develops into a severe infection characterized by acute respiratory distress syndrome (ARDS), and the condition of patients with severe illness may deteriorate to organ dysfunction and even death [1–4]. Globally, the World Health Organization (WHO) has reported over 150 million confirmed cases of COVID-19 as of May 11, 2021, including about 3.2 million deaths [5]. Therefore, early diagnosis of SARS-CoV-2 and prompt isolation of patients are the keys to prevent the further spread and outbreak of the virus. A rapid and accurate method for diagnosing SARS-CoV-2 in the field is urgently warranted.

Two main diagnostic methods for COVID-19 are currently in use: nucleic acid test and serological test. Virus nucleic acid real time-PCR (RT-PCR) is the standard method for the clinical diagnosis of SARS-CoV-2 [6–8]. Although RT-PCR can achieve early and ultrasensitive detection, it requires professional technicians and expensive instruments; moreover, the testing time is long. These disadvantages impede the application of RT-PCR in point-of-care testing (POCT) in the field. Detection of SARS-CoV-2 specific immunoglobulin (IgM and IgG) antibodies is a common POCT method for the diagnosis of COVID-19. However, studies have shown that specific IgM and IgG can only be detected at 2–3 weeks after SARS-CoV-2 infection [9–11]. Antibody detection is not suitable for the detection of asymptomatic patients and patients with early infection. Rapid antigen detection (RAD) is a type of POCT for specific antigens based on transverse flow assay (LFIA), which not only detects antigens in the early stages of infection, but also can be performed in a short period of time in the field [12,13]. Notably, selection of appropriate antigens is the key to rapid antigen detection of

* Corresponding author at: Beijing Institute of Radiation Medicine, Beijing 100850, PR China.
** Corresponding authors.
E-mail addresses: wangchongwen1987@126.com (C. Wang), zhaobaohua@mail.hebtu.edu.cn (B. Zhao), ruixiao203@sina.com (R. Xiao).

https://doi.org/10.1016/j.snb.2021.130897
Received 27 June 2021; Received in revised form 12 September 2021; Accepted 7 October 2021
Available online 9 October 2021

SARS-CoV-2. SARS-CoV-2 virus is a coronavirus with four major structural proteins: spikes, nucleocapsid proteins, membrane proteins, and envelope proteins. S protein is a very important surface protein of coronavirus, whose main function is to recognize host cell surface receptors and fuse with host cells and realize spread [1,4]. Therefore, S protein is a potential target for clinical diagnosis. In this study, a rapid antigen detection based on LFIA targeting S protein was selected.

Signal probe is an important part of LFIA system, among which colloidal gold is the traditional signal label. Colloidal gold-based (Au-based) LFIA test can be accomplished without professional technicians, and the results can be read visually. However, it has low sensitivity and poor quantitative ability [14,15]. Various composite nanoparticles have been explored as signal markers to overcome the drawbacks of Au-based LFIA and improve detection performance. Such markers include fluorescent microspheres, carbon-based nanoparticles (NPs), surface-enhanced Raman scattering (SERS) nanomaterials, up-converting phosphors, and many others [15–19]. As a new type of fluorescent materials, quantum dots (QDs) have been applied to LFIA systems. QDs have the advantages of high photostability, narrow fluorescence emission spectra, and quantifiable fluorescence intensity [14,17,20]. Nonetheless, the clinical application of QD-based LFIA has limitations owing to the small particle size of QDs (5–20 nm) and their poor biocompatibility [17]. Thus, QDs are assembled on carrier materials (such as Fe_3O_4, polymer, SiO_2, and latex) to prepare QD beads (QBs) [15,18–21]. Compared with QD-based LFIA, QB-based LFIA can produce a higher fluorescence signal and sensitivity [17,22,23]. What is noteworthy is that although QB-based LFIA has the capability of highly sensitive quantitative detection, the fluorescent material requires an additional excitation light source to observe the emitted light, which prevents POCT diagnosis from being applied in areas such as communities, schools, stations and other areas with poor medical resources.

In this study, we designed colorimetric fluorescent SiO_2@Au/QD NPs with dual functionality as novel signal tags for rapid and sensitive detection of SARS-CoV-2 S1 by naked eye/fluorescence dual modes. SiO_2@Au/QD is a typical core-shell structure material, which consists of mono-dispersed 200 nm SiO_2 as the core and a monolayer shell formed by mixing Au NPs and carboxyl QDs. For COVID-19 detection, our proposed SiO_2@Au/QD has three important advantages. Firstly, monodisperse SiO_2 cores ensure high stability of the material in complex solutions, thus allowing rapid detection of S-antigens in real biological samples without sample pretreatment. Secondly, the 20 nm Au NPs on the surface of the SiO_2 core can generate a strong colorimetric signal, which benefits the rapid diagnosis of suspicious samples in resource-poor areas without complicated instruments. Thirdly, the dense distribution of QDs in the Au interstitial space provides a powerful fluorescence signal of LFIA strip for more sensitive and accurate quantification of viral S antigen, which offers a possible way to improve the detection rate of SARS-CoV-2 infection in the field. In addition, QDs also provide rich carboxyl sites that facilitate efficient coupling of anti-SARS-CoV-2 antibodies on the surface of signal tags. Under optimal conditions, the limits of detection (vLOD) for SARS-CoV-2 S1 protein by colorimetric function of the proposed biosensor reached 1 ng/mL. Moreover, the limit of detection (LOD) for SARS-CoV-2 S1 using fluorescence function was 33 pg/mL. We also performed a scientifically exhaustive validation of the repeatability, specificity, and accuracy of the biosensor. It is worth noting that the biosensor based on SiO_2@Au/QDs has the advantages of simple synthesis method, low cost and mass production, which can be effectively applied to poor areas lacking advanced detection personnel and equipment. More importantly, the biosensor developed in this paper provides an effective method for rapid and accurate screening of SARS-CoV-2 infection and shows potential clinical applications.

2. Experimental section

2.1. Materials and reagents

SARS-CoV-2 spike 1 detection antibody (Catalog #40591-MM43), SARS-CoV-2 spike 1 capture antibody (Catalog #40150-D002), SARS-CoV-2 spike 1 protein (Catalog #40591-V08H) and SARS-CoV-2 (2019-nCoV) Spike Detection ELISA Kit (Cat: KIT40591) were purchased from Sino Biological Inc. (Beijing, China). For other materials and reagents, please read the Supporting information.

2.2. Instrumentation

Transmission electron microscope (TEM) images were captured by Hitachi H-7650 transmission electron microscope (TEM) at 150 kV operating voltage. The Philips Tecnai G2 F20 microscope captures high-resolution transmission electron microscope (HRTEM) images at 200 kV accelerating voltage. Scanning electron microscope (SEM) images were captured by JTOL JSM-7001 F microscope at 10 kV operating voltage.

The Shimadzu 2600 spectrometer mapped UV–vis spectra. Malvern Nano-ZS90 Zetasizer measured Zeta potential. The emission spectra of LFIA fluorescent strips based on QD were analyzed by FIC1-S1 fluorescent strip reader (Suzhou Hemai, China). FIC-S1 fluorescent strip reader recorded the fluorescence signal of SiO_2@Au/QD-based LFIA biosensor (Suzhou Hemai, China).

2.3. Preparation of dual-functional SiO_2@Au/QD NPs

As shown in Scheme 1a, SiO_2@Au/QD NPs with colorimetric-fluorescence dual-functional were synthesized by PEI self-assembly in three steps. First, 0.3 mL of SiO_2 NPs were homogeneously dispersed in an PEI aqueous solution (40 mL, 0.5 mg/mL), which rapidly formed a cationic layer on the surface of SiO_2 under sonication. After washing off the excess PEI by centrifugation after 40 min of ultrasound, the obtained SiO_2@PEI NPs were resuspended in 6 mL of deionized water. Second, 20 nm Au NPs (20 mL, 20 nM) were added to the SiO_2@PEI NPs and sonicate for 30 min to form SiO_2/Au NPs. The synthesized SiO_2/Au NPs were then purified by centrifugation (5500 rpm, 6 min) and dispersed in 30 mL of deionized water. Finally, SiO_2/Au NPs were mixed with 80 μL of carboxylate CdSe/ZnS-MPA QDs (10 μM) and incubated for 45 min under ultrasonic conditions resulting in the formation of SiO_2@Au/QD core-shell nanostructures with Au and QDs. Then, the purified SiO_2@Au/QD NPs were washed with deionized water by centrifugation (5200 rpm, 6 min) and stored in 15 mL of ethanol.

2.4. Preparation of labeled antibodies coupled to SiO_2@Au/QD for anti-S1 detection protein

The amide group of the anti-S1 detection antibody was coupled to the carboxyl site of SiO_2@Au/QDs by carbodiimide chemistry (Scheme 1b). The methods were as follows: 1 mL of SiO_2@Au/QDs was centrifuged and resuspended in 1 mL of MES buffer (0.1 M, pH 6.0). Next, EDC (10 mM, 100 μL) and NHS (100 mM, 20 μL) were added to the mixture under sonication for 15 min to activate the carboxyl groups of SiO_2@Au/QDs. The mixture was then purified by centrifugation and resuspended in 0.2 mL of 0.05% PBST solution (10 mM, pH 7.4), followed by incubation with 8 μg of anti S1 detection protein antibody for 2 h. Then, 100 μL of 10% skim milk was added to seal the unreacted carboxyl groups of SiO_2@Au/QD NPs. Finally, the immune-SiO_2@Au/QDs were washed twice by centrifugation with 0.05% PBST buffer. The final product was resuspended in PBS (10 mM, pH 7.4) for later use.

2.5. LFIA strip preparation for SARS-CoV-2 S1 protein detection

The LFIA strip consists of three separate components, including the sample pad, the nitrocellulose membrane (NC membrane) and the

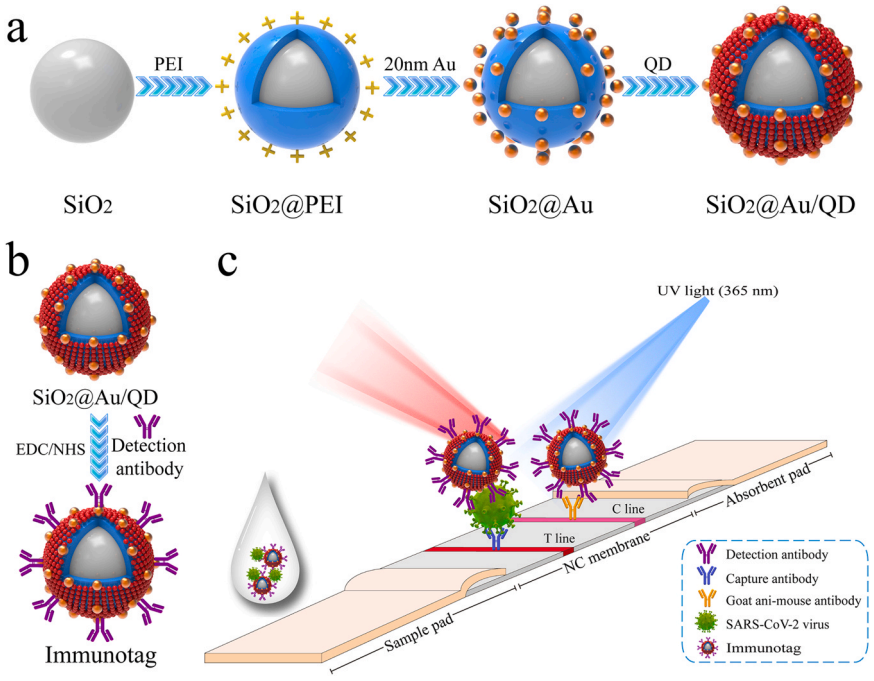

Scheme 1. (a) Sequential process for fabricating dual-functional SiO_2@Au/QD fluorescent labels. (b) Preparation of S protein-conjugated SiO_2@Au/QD labels. (c) Schematic of a dual-functional LFIA biosensor.

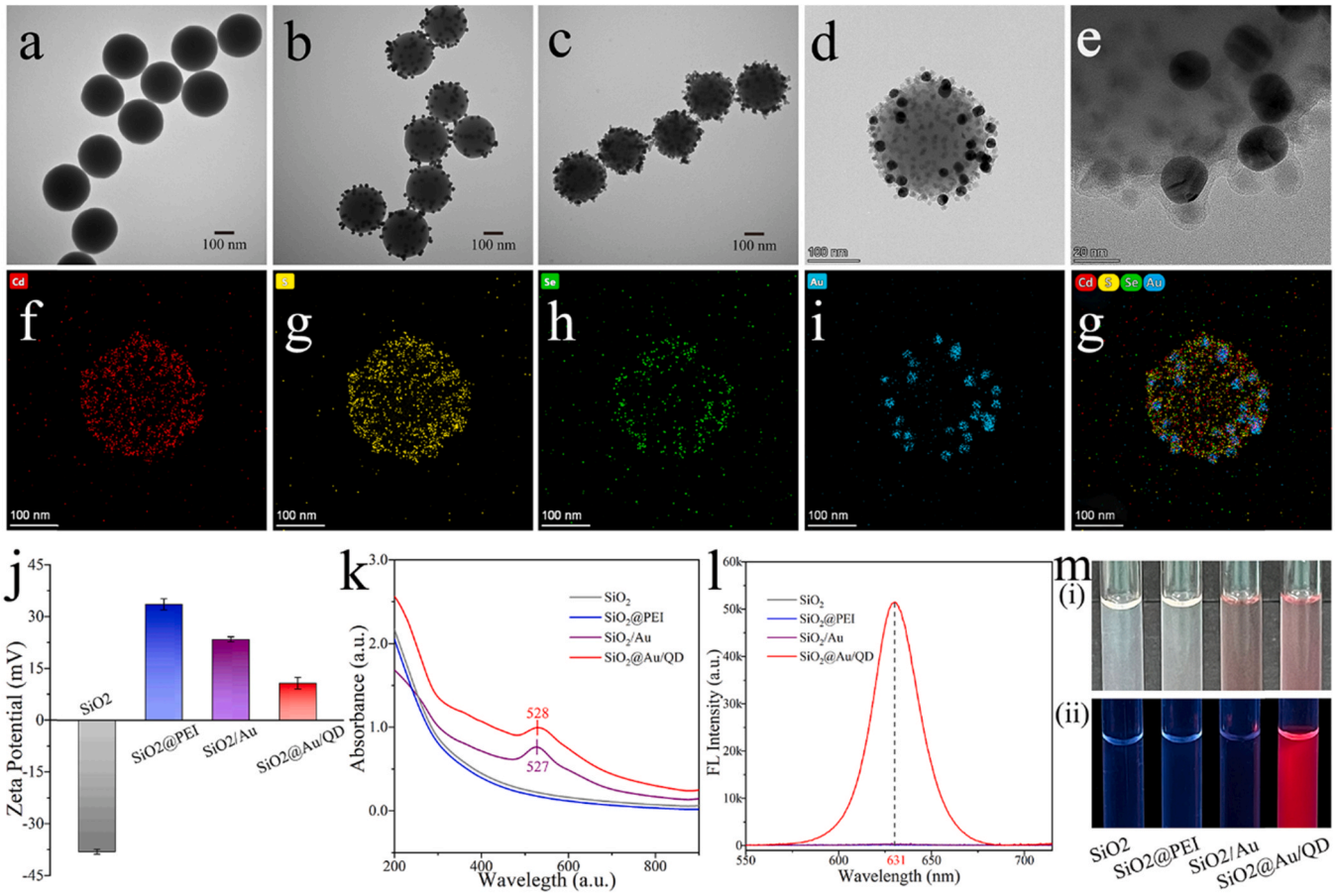

Fig. 1. TEM images of (a) SiO_2, (b) SiO_2/Au, and (c) SiO_2@Au/QD. HTEM images of (d) SiO_2@Au/QD and (e) Au lattice. Elemental mapping images (f and g) of the shell of SiO_2@Au/QD NP. (j) ζ-potential of the products at each stage. (k) Plasmon resonance spectra of SiO_2, SiO_2@PEI, SiO_2/Au, and SiO_2@Au/QD. (l) Fluorescence spectra of SiO_2, SiO_2@PEI, SiO_2/Au and SiO_2@Au/QD under UV light. (m) Photographs of sample plots of each phase product under (i) natural light and (ii) UV light.

absorbent pad (Scheme 1c). Two lines were sprayed on the NC membrane (CN140): the capture antibody (0.8 mg/mL) against SARS-CoV-2 S1 protein was sprayed onto the detection line (T line), and the goat anti-mouse IgG antibody (0.8 mg/mL) was coated onto the control line (C line), The membrane was dried at 37 °C for 2 h. Subsequently, three components were assembled onto the PVC base plate. Two kinds of pads respectively overlap the NC membrane by 1.5 mm to ensure a smooth transfer of the sample solution. The integrated membranes were cut into individual 3 mm strips, which were stored in a desiccator at room temperature for use in the assay.

3. Results and discussion

3.1. Preparation and characterization of SiO_2@Au/QD

The colorimetric-fluorescence dual-functional SiO_2@Au/QD NPs were synthesized by PEI-mediated LBL assembly strategy as illustrated in Scheme 1 in three steps: (i) SiO_2@PEI NPs were manufactured by PEI-mediated electrostatic adsorption to form PEI interlayers. (ii) Colloidal gold was adsorbed on part of the surface of SiO_2@PEI NPs to produce SiO_2/Au NPs. (iii) QDs adsorbed on the vacant sites of SiO_2/Au NPs to compound SiO_2@Au/QD NPs.

Transmission electron microscopy (TEM) and high resolution transmission electron microscopy (HRTEM), X-ray energy spectroscopy (EDS) and ζ-potential measurements are available for the characterization of SiO_2@Au/QD NPs. TEM images of SiO_2, SiO_2/Au, and SiO_2@Au/QD are shown in Fig. 1a–c, respectively. The shape of SiO_2 was nearly spherical, with a diameter of approximately 200 nm (Fig. 1a). SiO_2 displayed good monodispersity and stability, as well as produced abundant surface sites. Subsequently, 20 nm Au NPs were immobilized on the sites surface of SiO_2 to form an incomplete Au layer, whereas a part of the surface of the PEI coating remained exposed (Fig. 1b). The remaining sites of the PEI coating were occupied by negatively charged QDs through electrostatic interactions, resulting in SiO_2@Au/QD NPs with a mixed shell of Au and QD (Fig. 1c). As show in Fig. 1c, SiO_2@Au/QD NPs had a rough surface, good uniformity, and excellent dispersion. The magnified HRTEM image (Fig. 1d–e) exhibits that the small punctiform QDs were densely distributed in the SiO_2/Au interstices and the Au lattice with a grain size around 20 nm, these two images further explained the structure of SiO_2@Au/QD and the size of the nanoparticles. The results of EDS elemental mapping of the shell of SiO_2@Au/QD NPs are provided in Fig. 1f - g. The distributions of Cd (red), S (yellow), Se (green), and Au (blue) elements formed roughly a sphere, which confirmed the structural composition of the shell of SiO_2@Au/QD NPs. As is shown in Fig. 1j, the ζ-potential of SiO_2 measured with ζ-potential is − 38.1 mV, whereas that of the nanocomposite substantially increased to + 33.6 mV after PEI modification of SiO_2. However, after negatively charged Au NPs were adsorbed, the potential dropped to + 23.5 mV. Finally, negatively charged QD NPs filled the vacant sites of SiO_2@Au NPs, thereby further reducing the potential to + 10.8 mV. The regular variation in the ζ-potential was consistent with the electrostatic adsorption principle of LBL assembly, and this result confirmed the successful adsorption and assembly sequence of PEI, Au NPs, and QD NPs.

The dual-functional SiO_2@Au/QD NP materials possessed both colorimetric and fluorescent properties. The colorimetric property of the material was assessed. According to the UV–vis spectra (Fig. 1k), the SiO_2/Au curve had an obvious absorption peak at 527 nm, indicating that Au NPs had been successfully adsorbed on the surface of SiO_2@PEI NPs. As can be seen from the SiO_2@Au/QD curve, the UV–vis absorption peak of SiO_2/Au NPs did not remarkably change after the surface modification of QD NPs, indicating that the adsorption of QD did not affect the surface plasmonic resonance of SiO_2/Au. As shown in the Fig. 1m(i), SiO_2 NPs, SiO_2@PEI NPs, SiO_2/Au and SiO_2@Au/QDs were compared under natural light, SiO_2/Au and SiO_2@Au/QDs produced a purple-red color, indicating that they had normal colorimetric ability. The fluorescence property of SiO_2@Au/QD NPs was then evaluated. SiO_2 NPs, SiO_2@PEI NPs, and SiO_2/Au NPs did not exhibit fluorescence signals under 365 nm UV excitation conditions (Fig. 1l). By comparison, SiO_2@Au/QD NPs had a clear emission peak at 631 nm (Fig. 1l). These results indicated that sparse amounts of Au NPs did not affect the fluorescence radiation of SiO_2@Au/QD NPs nor caused metal quenching phenomenon. Photographs showing the state of different products under natural light and UV light are shown in Fig. 1m. Under natural light (Fig. 1m[i]), the solutions of SiO_2 NPs, SiO_2@PEI NPs were milky white and SiO_2@PEI NPs, SiO_2/Au NPs and SiO_2@Au/QD NPs showed purple-red color, indicating that SiO_2@Au/QD NPs had normal colorimetric ability. While, under 365 nm UV excitation conditions, only SiO_2@Au/QD NPs emitted fluorescence (Fig. 1m[ii]), indicating that SiO_2@Au/QDs had excellent fluorescence performance. In addition, SiO_2@Au/QD NPs preserved in ethanol showed little variation in fluorescence intensity over 60 days (Fig. S3a). SiO_2@Au/QD NPs in high-salt solution (1 M) did not agglomerate, whereas the conventional Au NPs caused severe aggregation in high-salt solution (Fig. S3b). The results of the comparison suggested that the new material had superior stability. The outstanding optical and chemical stability of SiO_2@Au/QD NPs were essential to ensure the reliability and sensitivity of the biosensor in complex samples.

3.2. Optimization of the shell composition of SiO_2@Au/QD

Given that the shell of SiO_2@Au/QD was constructed by mixing Au NPs and QD NPs, the material possessed both colorimetric and fluorescent properties. Different ratios of QDs and Au on the SiO_2 surface directly affected the fluorescence ability and the colorimetric intensity of the material. TEM images of SiO_2@Au/QD samples with Au-to-QD concentration ratios of 12.5%, 25%, 50%, and 75% were provided in Fig. 2a–d. With the increase of Au-to-QD concentration ratios, Au NPs on the surface of SiO_2 became denser, while the QDs absorbed decrease. Moreover, the colorimetric effect of SiO_2@Au/QD increased and the corresponding fluorescence intensity gradually decreased, as were shown in Fig. 2e(i) and e(ii). The UV absorption spectra of different materials at the same concentration but with different Au-to-QD concentration ratios were separately measured. The intensity of the UV absorption peaks increased as the Au-to-QD concentration ratio increased (Fig. 2f). The change in fluorescence intensity was opposite to that of UV absorption spectrum (Fig. 2g). The fluorescence intensity decreased as the Au-to-QD concentration ratios increased. Therefore, we need to find the balance between colorimetric signal and fluorescence signal.

SiO_2@Au/QDs with different Au-to-QD concentration ratios were made into an immune label to detect the SARS-CoV-2 S1 protein at a concentration of 1 ng/mL. As results were shown in the Fig. 2i, when the Au-to-QD concentration ratio was 12.5–75%, the colorimetric signal of the LFIA band based on SiO_2@Au/QDs was successively enhanced, while the fluorescence signal was weakened. As can be seen from the Fig. 2i(i), the colorimetric signals of LFIA bands with ratios of 12.5% and 25% were not obvious enough to be observed. Whereas, the colorimetric band was easily visible at the Au-to-QD concentration ratio of 50% and could be used for qualitative detection. Fluorescent signals of the strips were observed by a UV lamp in Fig. 2i(ii) and the fluorescent signals intensity on LFIA strips were measured (Fig. 2h). The detection results of 50% Au-to-QD concentration ratio achieved the highest signal-to-noise ratio (SNR). Hence, SiO_2@Au NPs with 50% Au-to-QD ratio was selected as the optimal material to achieve the best detection of colorimetric and fluorescent signals.

3.3. Construction and optimization of LFIA strips for antigen detection based on SiO_2@Au/QD

Scheme 1 described the preparation and operating principle of the SiO_2@Au/QDs-based LFIA biosensor for SARS-CoV-2 S1 protein detection. First, a capture antibody and a goat anti-mouse IgG antibody were

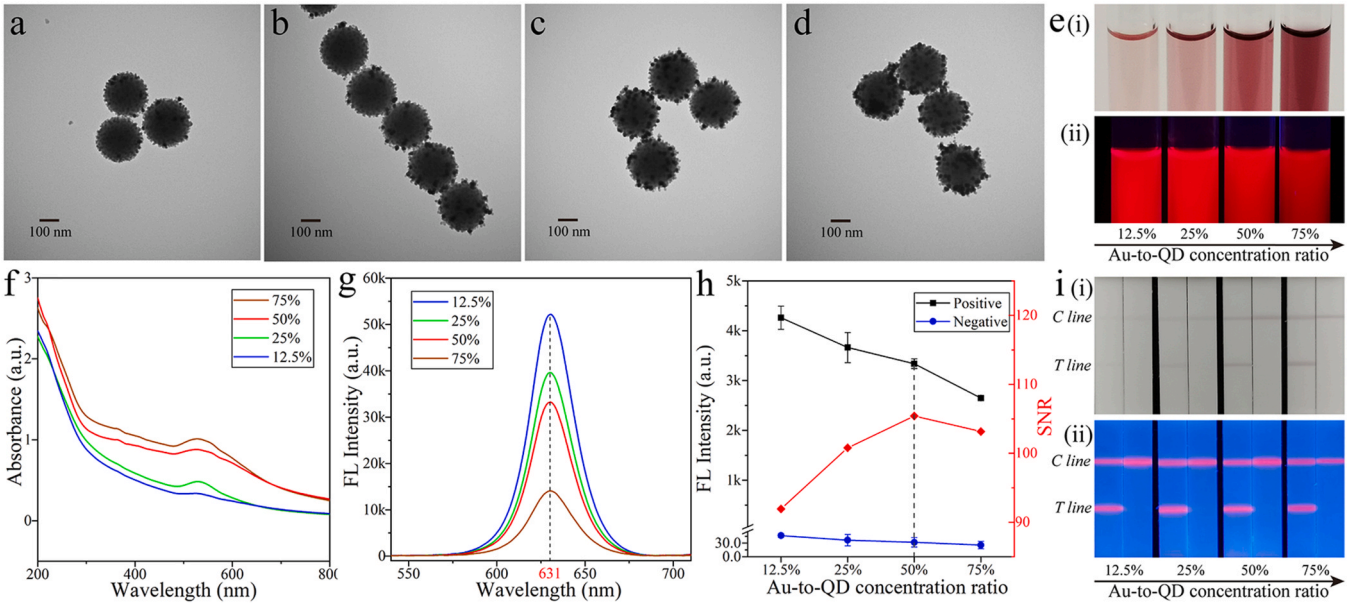

Fig. 2. TEM images of Au-to-QD concentration ratios of (a) 12.5%, (b) 25%, (c) 50%, and (d) 75%. (e) Photographs of SiO_2@Au/QD samples with Au-to-QD concentration ratios of 12.5%, 25%, 50%, and 75% under (i) natural light and (ii)UV light. (f) Plasmon resonance spectra of SiO_2@Au/QD samples with Au-to-QD concentration ratios of 12.5%, 25%, 50%, and 75%. (g) Fluorescence spectra of SiO_2@Au/QD samples with Au-to-QD concentration ratios of 12.5%, 25%, 50%, and 75% under UV light. (h) Effects of SiO_2@Au/QD with Au-to-QD concentration ratios of 12.5%, 25%, 50%, and 75% on LFIA strip. (i) Photographs of SiO_2@Au/QD-based LFIA with Au-to-QD concentration ratios of 12.5%, 25%, 50%, and 75% under [i] natural light and [ii] UV light.

sprayed on the detection line and the control line of LFIA, respectively. The S1 protein was then diluted to different concentrations with PBS, and the immune tag and the diluted proteins were added to the running buffer, where the S1 protein was immunologically bound to the detection antibody to form a SiO_2@Au/QD-S1 protein immune complex. Finally, the mixture was loaded onto the sample pad of the LFIA strip and moved in the direction of the absorbent pad with capillary action. When the immune complex reached the position of the test line, the S1 protein reacted with the capturing antibody. The residual SiO_2@Au/QD nanotags continued to migrate and were captured by the goat anti-mouse IgG fixed on the control line. Therefore, a bright colorimetric/fluorescence control line was observed, indicating that the LFIA strips were working properly. The test line showed colorimetric and fluorescent bands when the S1 protein was present in the sample, whereas no bands appeared on the test line in the absence of the S1 protein in the test sample.

Two aspects were optimized to achieve the best detection results: (i) optimization of the immune labels and (ii) optimization of the conditions of the LFIA system. First, immune tags were prepared by detection antibodies conjugated to carboxyl groups on the surface of SiO_2@Au/QDs via carbodiimide chemistry. The optimal amount of antibody to use was determined by modifying different amounts of the anti-S1 protein antibodies on activated SiO_2@Au/QDs and then measuring their zeta potential (Fig. S4a). The potential of immune SiO_2@Au/QDs decreased as the amount of the antibody increased (5–10 μg/mL) and stabilized at − 24 mV, indicating that the antibody on the surface of SiO_2@Au/QDs had reached the saturation state. The maximum loading capacity of the antibodies on SiO_2@Au/QDs was 8 μg/mL.

Next is the optimization of the conditions of the LFIA system. This assay was designed with the following key parameters as the starting points: type of NC membrane, reaction time, antibody concentration on the test line, composition of running buffer, and volume of immune label added. NC membranes with two pore sizes, namely, CN 95 (15 mm pore size) and CN 140 (8 mm pore size), were tested. Results showed that SiO_2@Au/QD NPs could be transported smoothly on both membranes. Given that CN140 had a smaller pore size than CN 95, the sample ran slower on the chromatographic strip, and its binding time with the detection line was longer. Thus, CN140 could produce a higher fluorescence detection signal than CN 95. Hence, CN140 was chosen as the ideal NC membrane in this experiment (Fig. S4b). It is worth mentioning that the detection results could be observed in 10 min, and the SNR reached the highest at 30 min (Fig. S5). Optimization of the other LFIA system conditions is described in Supporting information (Figs. S6–S8).

3.4. Sensitivity evaluation of dual-functional LFIA for detection of S1 protein

All optimized conditions were applied to detect SARS-CoV-2 S1 protein and evaluate the sensitivity of SiO_2@Au/QDs-based LFIA biosensor. The SARS-CoV-2 S1 protein was serially diluted from 1000 ng/mL to 0.05 ng/mL for eight concentrations and then loaded onto the strip biosensor. The control lines of all LFIA strips showed purple and fluorescent bands (Fig. 3b), indicating that the strip biosensor was working properly. The purple band was due to the local surface plasmon resonance effect of Au NPs, and the fluorescence band was revealed by the excitation of 356 nm UV light. No purple or fluorescent bands were detected on the test line (T line) of the blank, proving the reliability of the test results of the biosensor. As can be seen from Fig. 3b(i), the vLOD of S1 protein detected by SiO_2@Au/QD-LFIA colorimetric function was 1 ng/mL. Moreover, the visual sensitivity of fluorescence detection for S1 protein was 0.1 ng/mL (Fig. 3b[ii]). Fluorescence intensity on the T line was then recorded using a portable fluorometer, and a fitted curve (Fig. 3c) was plotted on the basis of the data obtained. The graph showed that fluorescence intensity was proportional to the concentrations of S1 proteins within the detection range of 0.05–1000 ng/mL. Based on the calibration curves, the LOD of fluorescence detection for S1 protein calculated by IUPAC standard method was 33 pg/mL ($LOD = y_{blank} + 3 \times SD_{blank}$, where y_{blank} is the mean signal intensity of blank group, and SD_{blank} is the standard deviation of the blank measurement). It has been reported that the average amount of S protein in saliva was estimated in the ρM range in most cases, and in severe cases in the nM range [7,25,26]. In this study, the vLOD of S protein detected by SiO_2@Au/QDs-LFIA colorimetric function was 0.02 nM. Moreover, the LOD of fluorescence detection for S protein was

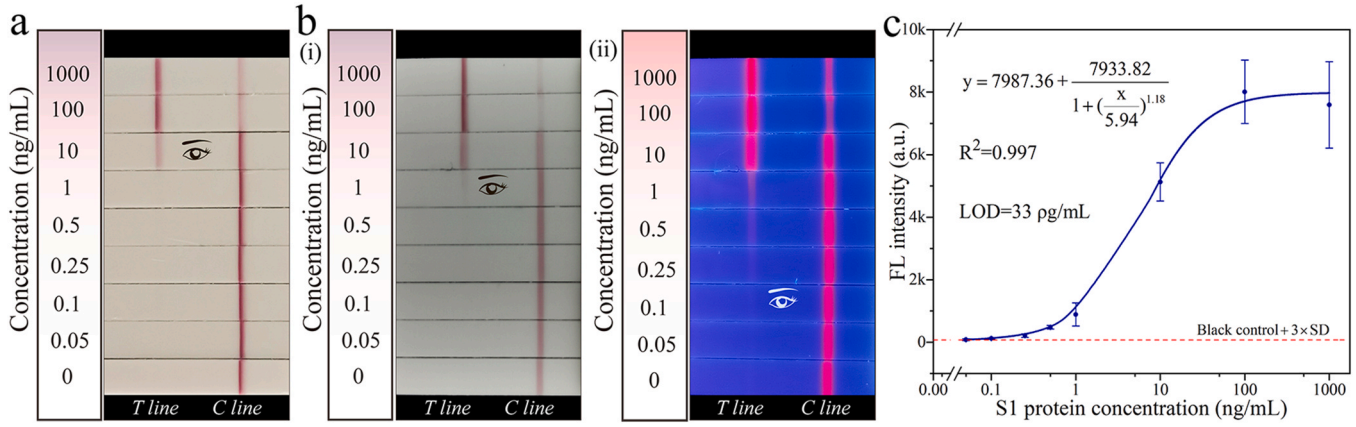

Fig. 3. (a) Photograph of Au NPs-based LFIA strips detection for different concentrations (0–1000 ng/mL) of S1 protein in running buffer. (b) Photographs of the SiO_2@Au/QD-based LFIA strips detection for different concentrations of S1 proteins (0–1000 ng/mL) in running buffer under (i) natural light and (ii) UV light. (c) The relationships of fluorescence intensities from T lines with the different concentration of S1 protein.

0.67 ρM. Therefore, our proposed biosensor can screen patients with different degrees of disease within a certain range.

In order to prove the superiority of our proposed method, we compared the detection performance of SiO_2@Au/QD-LFIA with the commonly used Au NPs-LFIA in the market. Under the same optimization conditions as SiO_2@Au/QD-LFIA, the vLOD of Au NPs-LFIA for S1 protein detection was 10 ng/mL (Fig. 3a). Hence, the vLOD of SiO_2@Au/QD-LFIA colorimetric function for S1 protein detection was 10 times that of Au NPs-LFIA by comparing Fig. 3a and c. Based on the calculated results of IUPAC standard method and Fig. 3a, the LOD of S1 protein detected by fluorescence function of SiO_2@Au/QD-LFIA was 300 times that of Au NPs-LFIA. Those results proved the excellent colorimetric and fluorescence detection capability of the bifunctional biosensor. In addition, the results of this study were also compared with previously reported results from other LFIA tests for SARS-CoV-2 antigens (Table 1).

3.5. Evaluation of repeatability, specificity, and simulated sample detection of dual-functional LFIA

As shown in Fig. 4a, the repeatability of SiO_2@Au/QD-LFIA was evaluated. The S1 protein was diluted into a high-dose group of 100 ng/mL and a medium-dose group of 1 ng/mL to perform five independent experiments. Purple and fluorescent bands were observed in both groups. Moreover, the relative standard deviation of fluorescence intensity was 6.89% and 7.16%, indicating that the prepared SiO_2@Au/QD-based LFIA strips had high reliability and repeatability. Next is the evaluation of the specificity of the SiO_2@Au/QD-based LFIA strips. Several respiratory viruses including SARS-CoV (100 ng/mL), MERS-CoV (100 ng/mL), H1N1 (5×10^6 copies/mL), Flu-B (5×10^4 copies/mL), RSV (5×10^5 pfu/mL) and ADV (5 μg/mL) were used as interferents to test the specificity of the biosensor (Fig. 4b). The color or signal of these six virus strains did not change, and only the SARS-CoV-2 group produced evident colorimetric and fluorescence signals, indicating that the LFIA band based on SiO_2@Au/QDs had good specificity. Finally, the accuracy of the biosensor in practical applications was evaluated by spiking the S1 protein into sputum and Tween (1%, V/V) mixture to simulate the detection of actual sample (Fig. 4c). The clinical samples were collected from the patient's throat and nose swab. The S1 protein was diluted into three concentrations of 100, 1, and 0.1 ng/mL, and the experiment was repeated three times. The recoveries corresponding to the three concentrations were 92.98%, 94.91%, and 99.26% (Table S1), respectively, indicating that the acceptable accuracy of novel biosensor for quantification of S1 proteins.

Table 1
Summary of the analytical performance of different methods to detect SARS-CoV-2.

Signal	Target	Signal mode	Limit of detection	Detection time (min)	Ref.
Colorimetric	S protein	One	1.86×10^5 copies/mL	20	Lee [25]
Chemiluminescence	S protein	One	0.1 ng/mL	16	Liu [26]
Colorimetric	N protein	One	0.65 ng/mL	20	Grant [27]
Colorimetric	N protein	One	2 ng/mL	20	Kim [28]
Fluorescence	N protein	One	5 pg/mL	15	Wang [29]
Colorimetric	S protein	One	0.1 nM	30	Hristov [30]
Fluorescence	S/NP Protein	One	1.6/2.2 ng/mL	10	Guo [31]
Colorimetric/ Fluorescence	S1 protein	Two	33 pg/mL	30	This work

3.6. Detection of SARS-CoV-2 real virus

The inactivated SARS-CoV-2 virus was provided by Prof. Chengfeng Qin (State Key Laboratory of Pathogen and Biosecurity, Beijing Institute of Microbiology and Epidemiology) [24]. The concentration of SARS-CoV-2 virions was quantified by real-time fluorescence quantitative PCR (qPCR). The sample of inactivated virus was diluted 5×10^5 times in the qPCR assay (Fig. S9a). A standard curve was drawn based on the cycle threshold and concentrations of the virus standard (Fig. S9b). According to the standard curve equation, the concentration of virions was calculated to be 7.06×10^8 copies/mL. In addition, the S proteins content of SARS-CoV-2 virions were quantified by commercial ELISA kits. Virus samples were diluted 300–38,400 times (Fig. S9c). The standard curve was made according to the concentration and optical density of protein standard substance (Fig. S9d). Then, the S protein content was calculated as 2.55 μg/mL according to the standard curve equation.

We detected inactivated viruses of SARS-CoV-2 to further verify the practical analytical capability of the new biosensor. SARS-CoV-2 inactivated virus were continuously diluted from 1.41×10^7 copies/mL to 7.06×10^3 copies/mL in 8 concentrations, and then virus diluents were dropped on the sample pads. All the tomographic strips showed C lines (Fig. 5a), proving that biosensors were working normally. It could be observed with the naked eyes that the limit of the detection for virions by SiO_2@Au/QD-LFIA colorimetric function was 7.06×10^5 copies/mL (Fig. 5a[i]). Base on the result of quantification for S proteins by ELISA,

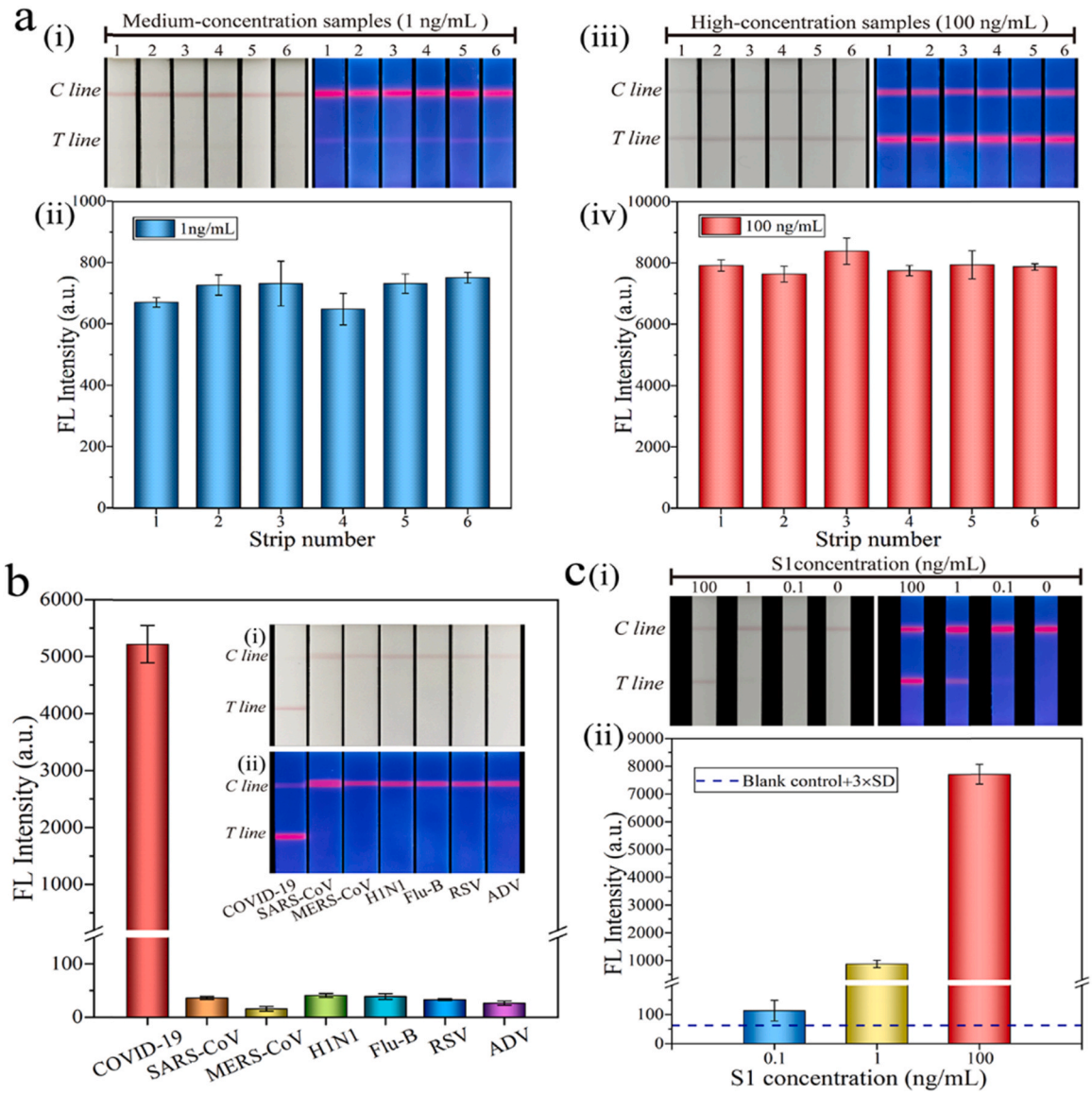

Fig. 4. (a) Assay reproducibility of SiO_2@Au/QD-based LFIA strips. Photographs of colorimetric and fluorescence at S1 proteins concentrations of (i) 1 ng/mL and (ii) 100 ng/mL, respectively. The fluorescence intensities corresponding to T line when S1 protein concentration was (iii) 1 ng/mL and (iv) 100 ng/mL, respectively. (b) Specificity of SiO_2@Au/QD-based LFIA strips in running buffer. Insets in (b) show photographs of the strips for several respiratory viruses under (i) natural light and (ii) UV light. (c) Accuracy of detection for S1 proteins by SiO_2@Au/QD-LFIA in saliva samples. (i) Colorimetric and fluorescence images of the detected S1 proteins in saliva samples. (ii) Corresponding test line fluorescence intensities of SiO_2@Au/QD-based LFIA detection for S1 proteins. For the detail, please refer to Table S1 in the Support information.

the concentration of S protein on the virus at vLOD was calculated to be 2.55 ng/mL. These results indicated that SiO_2@Au/QD-LFIA still had good performance in colorimetric detecting S proteins on real viruses. Notably, the visual sensitivity of fluorescence detection for S proteins on virions was 7.06×10^4 copies/mL (Fig. 5a[ii]). According to the results of portable fluorometer measurement and the fitting curve (Fig. 5b), the LOD of SiO_2@Au/QD-LFIA fluorescence detection for virions was calculated to be 1.02×10^4 copies/mL. Based on the results of ELISA, we calculated the LOD of S proteins on the inactivated viruses was 37 pg/mL, which was consistent with the detection sensitivity of standard S1 proteins indicating that SiO_2@Au/QD-LFIA had stable analytical ability in detecting real viruses.

Furthermore, the specificity and reliability of dual-function biosensor were evaluated by adding virions to saliva samples. We selected respiratory infectious viruses that cause symptoms similar to COVID-19 to verify the specificity of LFIA including H1N1 (5×10^6 copies/mL), Flu-B (5×10^4 copies/mL), ADV (5×10^5 pfu/mL) and RSV (5 μg/mL). As can be seen in Fig. 5c clear and bright bands appeared on the immunochromatographic strip only when SARS-CoV-2 virions were detected. While the false positives (non-specific binding) did not occur after the addition of high concentrations of interferers, which further proved the specificity of this detection method for COVID-19 detection. The accuracy of the biosensor in complex samples was also evaluated (Fig. 5d). We measured the fluorescence signal of T line and calculated the recoveries of positive samples. The recoveries for the mixtures of virions and saliva ranged from 93.63% to 98.02%, with low coefficient of variation (CV) ranging from 3.92% to 5.19% (Table S2). These results confirmed the novel biosensor has excellent accuracy and applicability for detection of SARS-CoV-2 in real samples.

4. Conclusions

In this paper, the synthesis of a novel colorimetric and fluorescent bifunctional SiO_2@Au/QDs was reported. This study was the first to

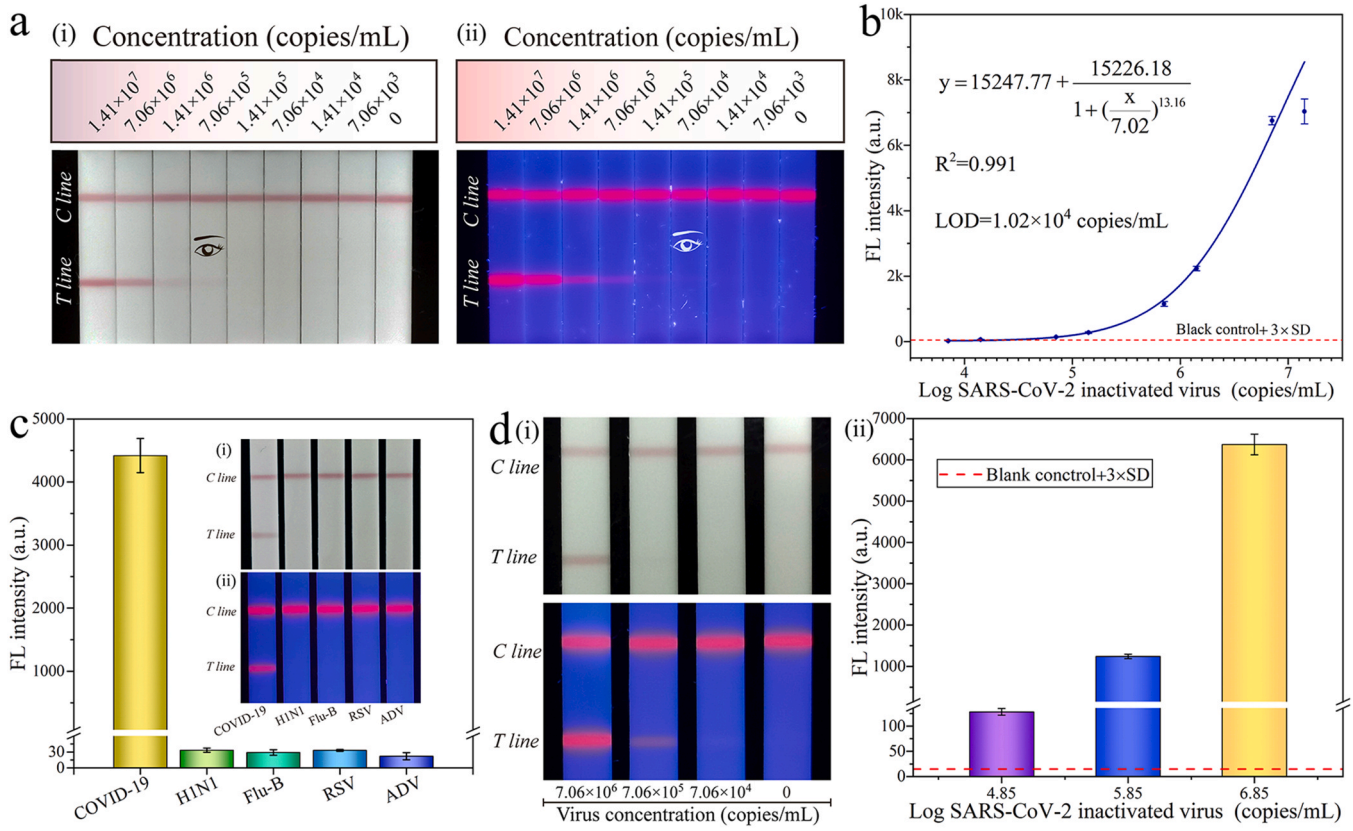

Fig. 5. (a) Photographs of the SiO_2@Au/QD-based LFIA strips detection for different concentrations of inactivated virus in running buffer under (i) natural light and (ii) UV light. (b) The relationships of fluorescence intensities from T lines with the different concentration of inactivated virus. (c) Specificity of SiO_2@Au/QD-based LFIA strips in saliva sample. Insets in (c) show photographs of the strips for several respiratory viruses under (i) natural light and (ii) UV light. (d) Accuracy of SiO_2@Au/QD-based LFIA bands in saliva samples. (i) Colorimetric and fluorescence images of the detected virions in saliva samples. (ii) Corresponding T line fluorescence intensities of SiO_2@Au/QD-based LFIA detection for virions. For the detail, please refer to Table S2 in the Support information.

introduce this new material into the LFIA system as a label for detecting the S1 protein of SARS-CoV-2. SiO_2@Au/QDs were prepared by coating a monolayer shell of Au and QDs onto a 200 nm SiO_2 core via PEI-mediated LBL assembly method. This kind of material displayed high dispersion and excellent stability with both colorimetric and fluorescence detection characteristics Under optimal conditions, the S1 protein of SARS-CoV-2 was detected by the SiO_2@Au/QD-based LFIA biosensor within 30 min. The detection limits of the detected S1 proteins using the colorimetric and fluorescence functions were 1 ng/mL and 33 pg/mL, respectively. In addition, the specificity, accuracy and real sample detection of the biosensor were fully validated. Therefore, the biosensor developed herein has the potential for rapid and accurate detection of SARS-CoV-2. In practical application, the colorimetric function of the new biosensor can make an on-site diagnosis without instruments for critically ill patients. Fluorescence mode allows highly sensitive and quantitative detection to screen patients with common symptoms. Moreover, the proposed SiO_2@Au/QDs-based LFIA system can be applied to rapid and sensitive diagnosis of other pathogens by using different specific antibodies and has a broad application prospect.

CRediT authorship contribution statement

Han Han: Methodology, Writing – original draft. **Chongwen Wang:** Conceptualization, Writing – review & editing. **Xingsheng Yang:** Methodology. **Shuai Zheng:** Methodology, Writing – original draft. **Xiaodan Cheng:** Methodology, Data curation. **Zhenzhen Liu:** Methodology. **Baohua Zhao:** Writing – review & editing. **Rui Xiao:** Funding acquisition, Writing – review & editing, Supervision.

Declaration of Competing Interest

The authors declare that they have no known competing financial interests or personal relationships that could have appeared to influence the work reported in this paper.

Acknowledgements

This study was supported by the Youth Development Program (Grant no. 21QNPY151).

Appendix A. Supplementary material

Supplementary data associated with this article can be found in the online version at doi:10.1016/j.snb.2021.130897.

References

[1] Y.J. Hou, K. Okuda, C.E. Edwards, D. Martinez, T. Asakura, K.H. Dinnon III, SARS-CoV-2 reverse genetics reveals a variable infection gradient in the respiratory tract, Cell 182 (2) (2020) 429–446.

[2] W.J. Guan, Z.Y. Ni, Y. Hu, W.H. Liang, C.Q. Ou, J.X. He, L. Liu, H. Shan, C.L. Lei, D. Hui, B. Du, L.J. Li, G. Zeng, K.Y. Yuen, R.C. Chen, C.L. Tang, T. Wang, P.Y. Chen, J. Xiang, S.Y. Li, J.L. Wang, Z.J. Liang, Y.X. Peng, L. Wei, Y. Liu, Y.H. Hu, P. Peng, J.M. Wang, J.Y. Liu, Z. Chen, G. Li, Z.J. Zheng, S.Q. Qiu, J. Luo, C.J. Ye, S.Y. Zhu, N.S. Zhong, China Medical Treatment Expert Group for Covid-19, Clinical characteristics of coronavirus disease 2019 in China, N. Engl. J. Med. 382 (2020) 1708–1720.

[3] L. Fu, B. Wang, T. Yuan, X. Chen, Y. Ao, T. Fitzpatrick, P. Li, Y. Zhou, Y.F. Lin, Q. Duan, G. Luo, S. Fan, Y. Lu, A. Feng, Y. Zhan, B. Liang, W. Cai, L. Zhang, X. Du, L. Li, Y. Shu, H. Zou, Clinical characteristics of coronavirus disease 2019 (COVID-19) in China: a systematic review and meta-analysis, J. Infect. 80 (2020) 656–665.

[4] A. Synowiec, A. Szczepański, E. Barreto-Duran, L.K. Lie, K. Pyrc, Severe acute respiratory syndrome coronavirus 2 (SARS-CoV-2): a systemic infection, Clin. Microbiol. Rev. 34 (2021) e00133-20.
[5] World Health Organization, COVID-19 Weekly Epidemiological Update, 2021. ⟨https://www.who.int/publications/m/item/weekly-epidemiological-update-on-covid-19/⟩. (Accessed 11 May 2021).
[6] Y.H. Jin, L. Cai, Z.S. Cheng, H. Cheng, T. Deng, Y.P. Fan, C. Fang, D. Huang, L. Q. Huang, Q. Huang, Y. Han, B. Hu, F. Hu, B.H. Li, Y.R. Li, K. Liang, L.K. Lin, L. S. Luo, J. Ma, L.L. Ma, Z.Y. Peng, Y.B. Pan, Z.Y. Pan, X.Q. Ren, H.M. Sun, Y. Wang, Y.Y. Wang, H. Weng, C.J. Wei, D.F. Wu, J. Xia, Y. Xiong, H.B. Xu, X.M. Yao, Y. F. Yuan, T.S. Ye, X.C. Zhang, Y.W. Zhang, Y.G. Zhang, H.M. Zhang, Y. Zhao, M. J. Zhao, H. Zi, X.T. Zeng, Y.Y. Wang, X.H. Wang, For the Zhongnan Hospital of Wuhan University Novel Coronavirus Management and Research Team, Evidence-Based Medicine Chapter of China International Exchange and Promotive Association for Medical and Health Care (CPAM), A rapid advice guideline for the diagnosis and treatment of 2019 novel coronavirus (2019-nCoV) infected pneumonia (standard version), Mil. Med. Res. 7 (2020) 4.
[7] R. Wölfel, V.M. Corman, W. Guggemos, M. Seilmaier, S. Zange, M.A. Müller, D. Niemeyer, T.C. Jones, P. Vollmar, C. Rothe, M. Hoelscher, T. Bleicker, S. Brünink, J. Schneider, R. Ehmann, K. Zwirglmaier, C. Drosten, C. Wendtner, Virological assessment of hospitalized patients with COVID-2019, Nature 581 (2020) 465–469.
[8] F. Cui, H.S. Zhou, Diagnostic methods and potential portable biosensors for coronavirus disease 2019, Biosens. Bioelectron. 165 (2020), 112349.
[9] Q.X. Long, B.Z. Liu, H.J. Deng, G.C. Wu, K. Deng, Y.K. Chen, P. Liao, J.F. Qiu, Y. Lin, X.F. Cai, D.Q. Wang, Y. Hu, J.H. Ren, N. Tang, Y.Y. Xu, L.H. Yu, Z. Mo, F. Gong, X.L. Zhang, W.G. Tian, L. Hu, X.X. Zhang, J.L. Xiang, H.X. Du, H.W. Liu, C. H. Lang, X.H. Luo, S.B. Wu, X.P. Cui, Z. Zhou, M.M. Zhu, J. Wang, C.J. Xue, X.F. Li, L. Wang, Z.J. Li, K. Wang, C.C. Niu, Q.J. Yang, X.J. Tang, Y. Zhang, X.M. Liu, J. J. Li, D.C. Zhang, F. Zhang, P. Liu, J. Yuan, Q. Li, J.L. Hu, J. Chen, A.L. Huang, Antibody responses to SARS-CoV-2 in patients with COVID-19, Nat. Med. 26 (2020) 845–848.
[10] X. Xu, J. Sun, S. Nie, H. Li, Y. Kong, M. Liang, J. Hou, X. Huang, D. Li, T. Ma, J. Peng, S. Gao, Y. Shao, H. Zhu, J.Y. Lau, G. Wang, C. Xie, L. Jiang, A. Huang, Z. Yang, K. Zhang, F.F. Hou, Seroprevalence of immunoglobulin M and G antibodies against SARS-CoV-2 in China, Nat. Med. 26 (2020) 1193–1195.
[11] H. Hou, T. Wang, B. Zhang, Y. Luo, L. Mao, F. Wang, S. Wu, Z. Sun, Detection of IgM and IgG antibodies in patients with coronavirus disease 2019, Clin. Transl. Immunol. 9 (2020), e01136.
[12] J. Sitjar, J.-D. Liao, H. Lee, H.-P. Tsai, J.-R. Wang, P.-Y. Liu, Challenges of SERS technology as a non-nucleic acid or -antigen detection method for SARS-CoV-2 virus and its variants, Biosens. Bioelectron. 181 (2021), 113153.
[13] M. Alafeef, K. Dighe, P. Moitra, D. Pan, Rapid, ultrasensitive, and quantitative detection of SARS-CoV-2 using antisense oligonucleotides directed electrochemical biosensor chip, ACS Nano (2020).
[14] A. Foubert, N.V. Beloglazova, S. De Saeger, Comparative study of colloidal gold and quantum dots as labels for multiplex screening tests for multi-mycotoxin detection, Anal. Chim. Acta 955 (2017) 48–57.
[15] A. Moyano, E. Serrano-Pertierra, M. Salvador, J.C. Martinez-Garcia, M. Rivas, M. C. Blanco-Lopez, Magnetic lateral flow immunoassays, Diagnostics 10 (2020).
[16] R. Banerjee, A. Jaiswal, Recent advances in nanoparticle-based lateral flow immunoassay as a point-of-care diagnostic tool for infectious agents and diseases, Analyst 143 (2018) 1970–1996.
[17] X. Yang, X. Liu, B. Gu, H. Liu, R. Xiao, C. Wang, S. Wang, Quantitative and simultaneous detection of two inflammation biomarkers via a fluorescent lateral flow immunoassay using dual-color SiO_2@QD nanotags, Mikrochim. Acta 187 (2020) 570.
[18] L. Shi, L. Xu, R. Xiao, Z. Zhou, C. Wang, S. Wang, B. Gu, Rapid, quantitative, high-sensitive detection of Escherichia coli O157:H7 by gold-shell silica-core nanospheres-based surface-enhanced Raman scattering lateral flow immunoassay, Front. Microbiol. 11 (2020).
[19] C. Wang, J. Wang, M. Li, X. Qu, K. Zhang, Z. Rong, R. Xiao, S. Wang, A rapid SERS method for label-free bacteria detection using polyethylenimine-modified Au-coated magnetic microspheres and Au@Ag nanoparticles, Analyst 141 (2016) 6226–6238.
[20] C. Wang, W. Shen, Z. Rong, X. Liu, B. Gu, R. Xiao, S. Wang, Layer-by-layer assembly of magnetic-core dual quantum dot-shell nanocomposites for fluorescence lateral flow detection of bacteria, Nanoscale 12 (2020) 795–807.
[21] L. Guo, Y. Shao, H. Duan, W. Ma, Y. Leng, X. Huang, Y. Xiong, Magnetic quantum dot nanobead-based fluorescent immunochromatographic assay for the highly sensitive detection of Aflatoxin B1 in dark soy sauce, Anal. Chem. 91 (2019) 4727–4734.
[22] Y. Shao, H. Duan, L. Guo, Y. Leng, W. Lai, Y. Xiong, Quantum dot nanobead-based multiplexed immunochromatographic assay for simultaneous detection of aflatoxin B1 and zearalenone, Anal. Chim. Acta 1025 (2018) 163–171.
[23] H. Duan, X. Huang, Y. Shao, L. Zheng, L. Guo, Y. Xiong, Size-dependent immunochromatographic assay with quantum dot, Anal. Chem. 89 (13) (2017) 7062–7068.
[24] N.N. Zhang, X.F. Li, Y.Q. Deng, H. Zhao, Y.J. Huang, G. Yang, W.J. Huang, P. Gao, C. Zhou, R.R. Zhang, Y. Guo, S.H. Sun, H. Fan, S.L. Zu, Q. Chen, Q. He, T.S. Cao, X. Y. Huang, H.Y. Qiu, J.H. Nie, Y. Jiang, H.Y. Yan, Q. Ye, X. Zhong, X.L. Xue, Z. Y. Zha, D. Zhou, X. Yang, Y.C. Wang, B. Ying, C.F. Qin, A thermostable mRNA vaccine against COVID-19, Cell 182 (2020) 1271–1283, e16.
[25] J.H. Lee, M. Choi, Y. Jung, S.K. Lee, C.S. Lee, J. Kim, J. Kim, N.H. Kim, B.T. Kim, H. G. Kim, A novel rapid detection for SARS-CoV-2 spike 1 antigens using human angiotensin converting enzyme 2 (ACE2), Biosens. Bioelectron. 171 (2021), 112715.
[26] D. Liu, C. Ju, C. Han, R. Shi, X. Chen, D. Duan, J. Yan, X. Yan, Nanozyme chemiluminescence paper test for rapid and sensitive detection of SARS-CoV-2 antigen, Biosens. Bioelectron. 173 (2020), 112817.
[27] B.D. Grant, C.E. Anderson, J.R. Williford, L.F. Alonzo, V.A. Glukhova, D.S. Boyle, B. H. Weigl, K.P. Nichols, SARS-CoV-2 coronavirus nucleocapsid antigen-detecting half-strip lateral flow assay toward the development of point of care tests using commercially available reagents, Anal. Chem. 92 (2020) 11305–11309.
[28] H.Y. Kim, J.H. Lee, M.J. Kim, S.C. Park, M. Choi, W. Lee, K.B. Ku, B.T. Kim, E. Changkyun Park, H.G. Kim, S.I. Kim, Development of a SARS-CoV-2-specific biosensor for antigen detection using scFv-Fc fusion proteins, Biosens. Bioelectron. 175 (2021), 112868.
[29] C. Wang, X. Yang, S. Zheng, X. Cheng, R. Xiao, Q. Li, W. Wang, X. Liu, S. Wang, Development of an ultrasensitive fluorescent immunochromatographic assay based on multilayer quantum dot nanobead for simultaneous detection of SARS-CoV-2 antigen and influenza A virus, Sens. Actuators B Chem. 345 (2021), 130372.
[30] D. Hristov, H. Rijal, J. Gomez-Marquez, K. Hamad-Schifferli, Developing a paper-based antigen assay to differentiate between coronaviruses and SARS-CoV-2 spike variants, Anal. Chem. 93 (2021) 7825–7832.
[31] J. Guo, S. Chen, S. Tian, K. Liu, J. Ni, M. Zhao, Y. Kang, X. Ma, J. Guo, 5G-enabled ultra-sensitive fluorescence sensor for proactive prognosis of COVID-19, Biosens. Bioelectron. 181 (2021), 113160.

Han Han is a master student at College of Life Science, Hebei Normal University. Her work focuses on development of nanoparticle-based biosensors.

Chongwen Wang is currently an associate professor at Anhui Agricultural University in China. His research focuses on molecular diagnostic technology, biosensing technology, and rapid detection of pathogenic microorganisms.

Shuai Zheng is a doctoral student at Anhui Agricultural University in China. His research interests include new techniques for immunochromatographic detection.

Xingsheng Yang is a master student at Anhui Agricultural University in China. His work focuses on the development of nanoparticle-based biosensors.

Xiaodan Cheng is a master student at Anhui Agricultural University in China. His work focuses on the development of nanoparticle-based biosensors.

Zhenzhen Liu is a master student under the guidance of Dr. Rui Xiao at the Beijing Institute of Radiation Medicine. Her work focuses on the development of nanoparticle-based biosensors.

Rui Xiao is currently an associate professor at the Beijing Institute of Radiation Medicine. Beijing Institute of Radiation Medicine. Her research interests include SERS-based biosensors and SERS materials fabrication.

Baohua Zhao is currently a professor at the College of Life Science, Hebei Normal University. His research focuses on molecular pathogenic mechanisms of pathogenic microorganisms and prevention.